Characterization of induced nanoplasmonic fields in time-resolved photoemission: A classical trajectory approach applied to gold nanospheres

Erfan Saydanzad, Jianxiong Li, and Uwe Thumm
Department of Physics, Kansas State University, Manhattan, Kansas 66506, USA
(Received 2 February 2017; published 15 May 2017)

Attosecond time-resolved spectroscopy has been shown to be a powerful method for examining the electronic dynamics in atoms, and this technique is now being transferred to the investigation of elastic and inelastic scattering during electron transport and collective electronic (plasmonic) effects in solids. By sampling over classical photoelectron trajectories, we simulated streaked photoelectron energy spectra as a function of the time delay between ionizing isolated attosecond extreme ultraviolet (XUV) pulses and assisting infrared or visible streaking laser pulses. Our calculations comprise a sequence of four steps: XUV excitation, electron transport in matter, escape from the surface, and propagation to the photoelectron detector. Based on numerical applications to gold nanospheres of 5- and 50-nm radius, we investigate streaked photoemission spectra with regard to (i) the nanoparticle's dielectric response to the electric field of the streaking laser pulse, (ii) relative contributions to photoelectron release from different locations on the surface and inside the nanoparticle, (iii) contributions of photoemission from the Fermi level only versus emission from the entire occupied conduction band, and (iv) their fidelity in imaging the spatiotemporal distribution of the induced plasmonic field near the particle's surface.

DOI: 10.1103/PhysRevA.95.053406

I. INTRODUCTION

Starting with the new millennium, attosecond science has made rapid progress in developing pump-probe techniques for investigating the dynamics of electronic processes at the natural time scale of the electronic motion in matter, 1 as (1 attosecond $=10^{-18}$ s). After a decade of proof-of-principles applications to relative simple systems, such as atoms in the gas phase, this field of research is now further expanding to include time-resolved investigations of electronic excitation, electron transport, and collective electronic processes in solid matter [1,2]. In particular, the combination of attosecond ultrashort-pulse-laser technology with recent advances in nanoscience and nanotechnologies holds promise for the understanding and detailed characterization, design, and fabrication of novel nanometer-scale structures that respond to irradiation with intense electromagnetic radiation in a controllable way, promoting, for example, new applications of ultrafast electro-optical information processing [2,3].

The response of matter to an incident pulse of electromagnetic radiation originates in the incident-field-driven coherent collective motion of valence electrons. This induced polarization in turn generates an induced "plasmonic" field. Close to the surface of subwavelength-size metallic nanostructures that are stimulated near their natural resonance (plasmon) frequency, the induced plasmonic response can be very strong. Near nanostructured surfaces [4–10] and isolated nanoparticles [11,12] the induced plasmonic (near) field can exceed the local intensity of the incident inducing field by orders of magnitude. Near noble-metal nanoparticles driven at the plasmon-resonance frequency, the local plasmonic-field-intensity enhancement can be as large as 10^4 [13], and for Au surfaces covered with random scatterers, local enhancements of second-harmonic generation near Au and Ag island films of three orders of magnitude were observed [14]. The strong plasmonic response near nanostructured surfaces has been exploited for some time in well-established surface-enhanced Raman spectroscopy (SERS) [15] and constitutes the enabling concept in several prototype and suggested applications, including time-resolved nanoplasmonic-field microscopy [4], nanoplasmonically enhanced photocatalysis [16], and efficient light harvesting [17]. For noble-metal substrates, the plasmonic-field enhancement of the incident and Raman-scattered light can increase the Raman signal dramatically, by more than a factor of 10^9, enabling SERS of single molecules [15].

The desire to understand, image, and ultimately control plasmonic excitations in solids motivates the continued improvement of imaging techniques towards the spatiotemporal resolution of plasmonic field distributions [4,18]. A very promising way to realize the detailed mapping of induced plasmonic fields with atomic resolution in time and space appears to be photoelectron streaking spectroscopy [18]. Applied to solid targets, such high-resolution photoemission studies on extended targets address effects that are absent in isolated atoms in the gas phase. These additional phenomena include the propagation of photoreleased electrons in the solid from their release point to the surface, subject to elastic and inelastic scattering [19,20], the emitted photoelectron's interaction with equilibrating residual surface-charge distributions [21], its interaction with the spatially inhomogeneous plasmonic field [11,12,18,22–25], and the finite skin depth [20] of the incident pulses of electromagnetic radiation.

Motivated by the need for unraveling the imprints of these effects on streaked photoemission spectra, the present work investigates the strong transient polarization of subinfrared (sub-IR)-wavelength-size gold nanospheres by an intense IR or visible pulse (Fig. 1; in the following text we refer to "IR" as including the visible spectral range). For linearly polarized incident IR pulses, the induced polarization resulting from the coherent driven motion of a large number of gold conduction electrons oscillates with the IR laser carrier frequency and generates the surface-enhanced inhomogeneous plasmonic field. The driving IR and induced field are shifted by a phase that depends on the detuning of the IR-laser frequency from the plasmon resonance frequency of the nanoparticles.

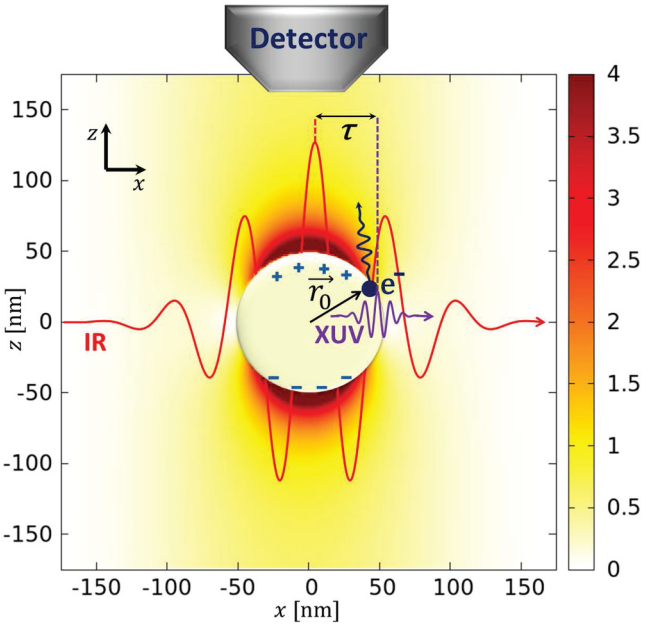

FIG. 1. Illustration of attosecond streaking spectroscopy of nanospheres. Photoelectrons are excited by an isolated XUV pulse at initial positions $\vec{r}_0$ with velocities $\vec{v}_0$. Upon leaving the nanosphere they experience the plasmonically enhanced field of the delayed IR streaking pulse. τ designates the time delay between the IR and XUV pulse.

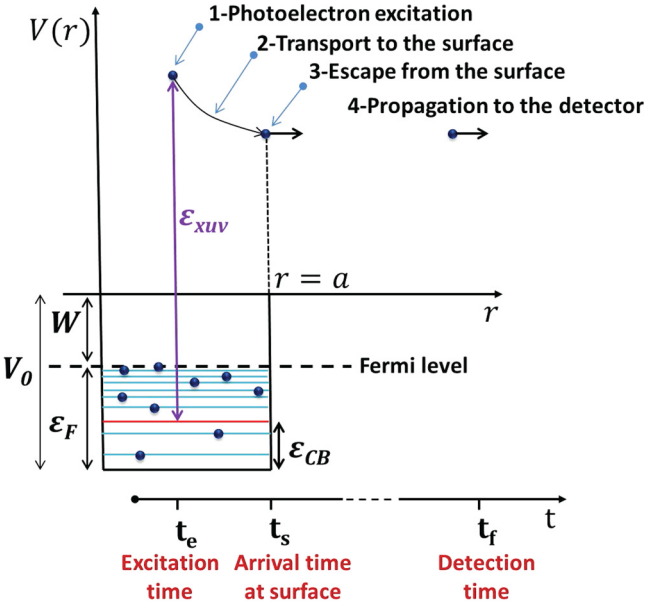

FIG. 2. Schematics of IR-streaked single-photon XUV photoemission from the occupied conduction band of a nanosphere.

In this work, we probe the plasmonic response of nanoparticles by single-XUV-photon emission of gold conduction electrons in the electric field of delayed ultrashort IR (or visible) pulses. During this laser-assisted XUV photoemission process, the streaking pulse thus has two distinct functions, as it both stimulates and probes the dielectric plasmonic response of the nanospheres. Photoelectrons released by the XUV pulse propagate inside the nanoparticle and are subject to elastic and inelastic collisions with electrons and nuclei of the nanosphere. Upon reaching the surface, they may get emitted and experience the net electric field of the streaking pulse and induced plasmonic field before possibly moving a macroscopic distance to the time-of-flight detector that registers their momentum for a given delay between the streaking pulse and ionizing single-attosecond XUV pulse.

The described scenario is illustrated in Fig. 2 and can be thought of as a sequence of four distinct steps: (1) excitation of the photoelectron by the XUV pulse at time t_e, (2) transport of the excited photoelectron to the surface during the time interval $t_s - t_e$, (3) escape of the photoelectron from the surface at time t_s, and (4) propagation of the released electron to the detector during the time interval $t_f - t_s$.

In our theoretical modeling of streaked photoemission from nanoparticles we assume Gaussian XUV pulses with central energy $\varepsilon_{\rm xuv}^{\rm ctr} = 105$ eV and full temporal width at half intensity maximum (FWHIM) $\Delta t_{\rm xuv} = 287$ as, represented by the electric field

$$\vec{E}_{\rm xuv}(\vec{r},t) = \vec{E}_{\rm xuv,0}\exp\left(-2\ln 2\frac{\left(t-k_{\rm xuv}x/\varepsilon_{\rm xuv}^{\rm ctr}\right)^2}{\Delta t_{\rm xuv}^2}\right) \times \exp\left[-i\left(\varepsilon_{\rm xuv}^{\rm ctr}t - k_{\rm xuv}x\right)\right], \quad (1)$$

with $k_{\rm xuv} = \varepsilon_{\rm xuv}/c$ and the speed of light in vacuum c. We further assume streaking pulses with Gaussian temporal profile,

$$\vec{E}_{\rm inc}(\vec{r},t) = \vec{E}_{\rm IR,0}\exp\left(-2\ln 2\frac{\left(t+\tau-\frac{kx}{\omega}\right)^2}{\Delta t_{\rm IR}^2}\right) \times \exp\{-i[\omega(t+\tau)-kx+\pi]\}, \quad (2)$$

pulse length (FWHIM) $\Delta t_{\rm IR} = 2.472$ fs, $\lambda_{\rm IR}^{\rm ctr} = 2\pi/k = 2\pi c/\omega = 720$ and 530 nm central wavelength, and 10^{12} W/cm^2 peak intensity. The time delay τ between the XUV and the IR pulses we define to be positive if the IR pulses precede the XUV pulses. Both pulses are linearly polarized along the z axis and propagate along the positive x axis of our Cartesian coordinate system (Fig. 1). Based on the small cross section for XUV photoemission from gold nanoparticles [26], we assume the nanoparticle to be transparent to the XUV pulses. Unless stated otherwise, we use atomic units ($\hbar = e = m_e = 1$) throughout this work.

II. THEORY

A. Induced plasmonic electric field

We model the conduction band of the nanosphere based on a spherical square-well potential with radius a and depth $V_0 = \varepsilon_F + W$, where $\varepsilon_F = 5.53$ eV is the Fermi energy [27] and $W = 5.1$ eV the work function for bulk gold [28] (Fig. 2). Expressing the oscillating induced dipole moment of the nanosphere,

$$\vec{P}(t) = (2\pi)^{-1/2}\int_{-\infty}^{\infty} d\omega e^{i\omega t}\vec{P}(\omega),$$
$$\vec{P}(\omega) = \epsilon_0\epsilon_m\alpha(\omega)\vec{E}_{\rm inc}(\vec{r},\omega), \quad (3)$$

in terms of the complex polarizability $\alpha(\omega)$, the spectral components of the incident streaking pulse (2), $\vec{\tilde{E}}_{\rm inc}(\vec{r},\omega)$, and

the relative permittivity of the surrounding medium (vacuum) ϵ_m (=1), the induced plasmonic field generated by $\vec{P}(t)$ is given by [29]

$$\vec{E}_{\rm pl}(\vec{r},t) = \frac{1}{\epsilon_m}\left(k^2[\hat{r}\times\vec{P}(t)]\times\hat{r}\frac{e^{ikr}}{r} + \{3\hat{r}[\hat{r}\cdot\vec{P}(t)] - \vec{P}(t)\}\left(\frac{1}{r^3}-\frac{ik}{r^2}\right)e^{ikr}\right), \quad (4)$$

where $\hat{r}$ is a unit vector in the direction of $\vec{r}$. The dipole approximation underlying this expression is justified by the nanoparticle radii in our numerical examples below not exceeding 50 nm and thus being significantly smaller than the wavelength of the streaking pulse [30].

In order to explain the colors of colloidal gold particles in solution, Mie in 1908 applied classical electrodynamics to the scattering and absorption of electromagnetic radiation by dielectric spheres [31]. Following Mie's approach, for radii $a < 0.1\lambda_{\rm IR}^{\rm ctr}$ the complex polarizability of the nanosphere can be written as [32]

$$\alpha(\omega) = \frac{9 - 0.9[\epsilon(\omega)+\epsilon_m]s^2 + O(s^4)}{3 + 9\epsilon_m/[\epsilon(\omega)-\epsilon_m] - [0.3\epsilon(\omega)+3\epsilon_m]s^2 - i2\epsilon_m^{3/2}s^3 + O(s^4)}V \quad (5)$$

in terms of expansions of the numerator and denominator in the dimensionless size parameter $s = 2\pi a/\lambda_{\rm IR}^{\rm ctr}$, the frequency-dependent dielectric function $\epsilon(\omega)$, and the volume of the nanosphere, $V = (4/3)\pi a^3$. While a square-well potential is obviously a crude representation of a nanosphere's valence electronic structure, our sampling over all occupied conduction-band states and the XUV-pulse spectral profile (discussed below) tends to average over details in the target's band structure, which we thus assume to be of secondary relevance to the description of currently observable streaked photoelectron spectra. For the numerical example discussed below, the maximal value of s is $s_{\rm max} = 0.57$, justifying our neglect of terms of the order s^4 and higher orders.

While $\alpha(\omega)$ is calculated for the specific (spherical) symmetry and depends on the size of our target, we represent the dielectric function in Eq. (5) within the Drude-Lorentz model [33,34] for bulk gold in closed analytical form as

$$\epsilon(\omega) = \epsilon_\infty - \frac{\omega_{pl}^2}{\omega(\omega+i\gamma_{\rm pl})} + \sum_{p=1}^{2} A_p\Omega_p\left(\frac{e^{i\phi_p}}{\Omega_p-\omega-i\Gamma_p} + \frac{e^{-i\phi_p}}{\Omega_p+\omega+i\Gamma_p}\right). \quad (6)$$

The two first terms constitute the standard Drude model [27,35] with the high-frequency-limit dielectric function $\epsilon_\infty = 1.1431$, plasma frequency $\omega_{\rm pl} = 1.3202\times10^{16}$ rad/s, and plasmon damping constant $\gamma_{\rm pl} = 1.0805\times10^{14}$ rad/s. The remaining terms in Eq. (6) relate to interband transitions which are represented by Lorentz oscillators with oscillator strengths $\Omega_1 = 3.8711\times10^{15}$ and $\Omega_2 = 4.1684\times10^{15}$ rad/s, spectral widths $\Gamma_1 = 4.4642\times10^{14}$ and $\Gamma_2 = 2.3555\times10^{15}$ rad/s, amplitudes $A_1 = 0.26698$ and $A_2 = 3.0834$, and phases $\phi_1 = -1.2371$ and $\phi_2 = -1.0968$. The parameters Ω_p, Γ_p, A_p, and ϕ_p are obtained in Ref. [36] by fitting experimental optical data for bulk gold. Since in our numerical applications the streaking pulses are sufficiently long to have very small spectral widths, we can ignore the variation of $\epsilon(\omega)$ with ω and instead employ its value at the central frequency $2\pi c/\lambda_{\rm IR}^{\rm ctr}$ of the streaking pulse as a dielectric constant.

The enhancement of the net electric field near the nanosphere surface varies with the degree of latitude and is largest at the poles, the poles $\vec{r}_p = (0,0,\pm a)$ being defined with regard to the polarization direction of the IR pulses. Figure 3 shows the plasmonic-field enhancement

$$\eta_{\rm pole}(\lambda_{\rm IR}^{\rm ctr}) = |\vec{E}_{\rm inc} + \vec{E}_{\rm pl}|/|\vec{E}_{\rm inc}| \quad (7)$$

as a function of the streaking-pulse wavelength for nanospheres with radii between 5 and 50 nm. As expected from a simple box-quantization consideration, $\eta_{\rm pole}(\lambda_{\rm IR}^{\rm ctr})$ sensitively depends on the nanoparticle size, and its maximum redshifts as the particle size increases.

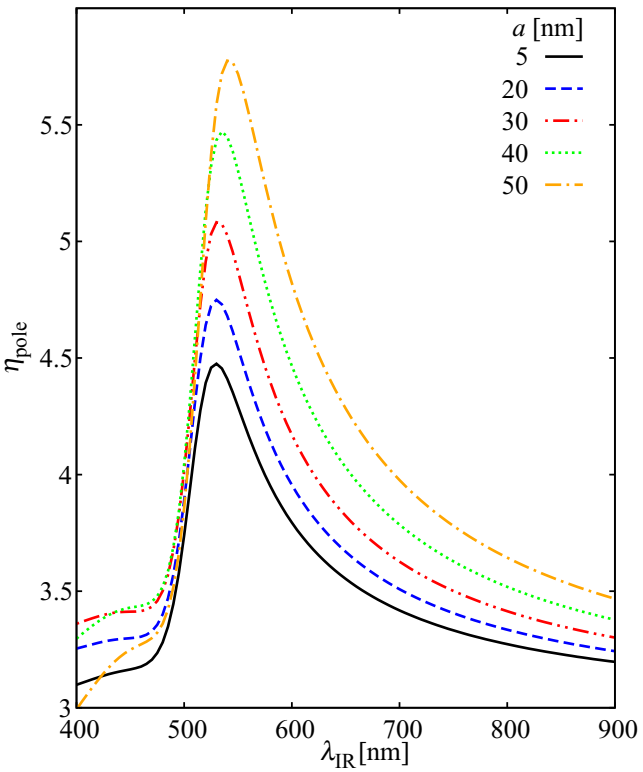

FIG. 3. Plasmonic-field enhancement at the poles of gold nanospheres of different radii a as a function of the wavelength $\lambda_{\rm IR}^{\rm ctr}$ of the incident 10^{12} W/cm^2 peak intensity pulse.

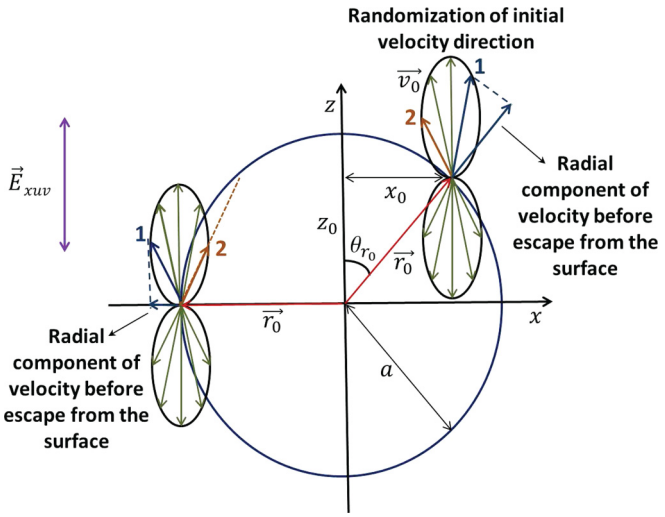

FIG. 4. Schematics for the excitation time calculation and illustration of the "surface effect" (blue vectors labeled with 1) and "transport effect" (brown vectors labeled with 2) for two different points on the surface of the nanosphere.

B. Trajectory calculation

Following the four-step sequence of photoelectron excitation, transport, escape, and propagation to the detector illustrated in Fig. 2, we numerically calculate photoelectron trajectories for given initial positions $\vec{r}_0$ and initial velocities $\vec{v}_0$.

1. Excitation

We define our time scale by assuming the center of the XUV pulse to pass the $x = 0$ plane at time zero (Fig. 1) and refer to the "excitation time" $t_e = x_0/c$ as the instant when a conduction electron is excited and released by absorption of a single XUV photon at an excitation point $\vec{r}_0 = (x_0, y_0, z_0)$ inside the nanoparticle. This time is different for different excitation positions and equal to the propagation time of the XUV pulse between the reference plane at $x = 0$ and the excitation point (Fig. 4). The delayed excitation is specific to our classical modeling of the photoemission process. While it is negligible for photoemission from atoms, the travel time of XUV light across the largest nanospheres of 50-nm radius studied in our numerical examples below is 334 as. Accounting for delays between the XUV excitation of conduction electrons at different locations is therefore crucial for our calculation of attosecond time-resolved streaking spectra.

2. Transport to the surface

After excitation, the photoelectron propagates inside the nanoparticle towards the surface, changing its momentum and losing kinetic energy due to elastic and inelastic collisions. We refer to this change of the photoelectron's propagation direction and energy as the "transport effect." We include this effect in both calculating individual electron trajectories and sampling over trajectories (cf. Sec. II C 3 below).

In the numerical examples discussed in Sec. III below, released photoelectrons propagate inside the nanoparticle with kinetic energies between approximately 85 and 110 eV. In this energy range, the inelastic mean free path (IMFP) λ_i varies insignificantly by about 1% and is considered as a constant value of 0.441 nm [37].

We model transport effects inside the nanoparticle on individual electron trajectories within the Drude model for metals [27] by introducing the frictional damping force

$$\vec{F}(\vec{v}) = -m^*\vec{v}/\tau_{\text{relax}} \tag{8}$$

in Newton's equation of motion

$$m^*\frac{d}{dt}\vec{v}(\vec{r},t) = \vec{F}(\vec{v}), \quad r < a, \tag{9}$$

where $m^* = 1.1$ is the effective electron mass [27]. The relaxation time of bulk gold conduction electrons is $\tau_{\text{relax}} = \lambda_i/v_F = 30$ fs, with respect to the Fermi velocity $v_F = 1.40\times10^8$ cm/s [27]. Since gold is a good conductor, the electric field inside the nanosphere is negligible and therefore absent in Eq. (9). For a given initial point $(\vec{r}_0, \vec{v}_0)$ in phase space, the position and velocity of the released electron inside the nanoparticle as a function of time then immediately follow from Eq. (9) as

$$\begin{aligned}\vec{v}(t) &= \vec{v}_0 e^{-\left(\frac{t-t_b}{\tau_{\text{relax}}}\right)},\\ \vec{r}(t) &= \vec{r}_0 + \tau_{\text{relax}}\vec{v}_0\left[1 - e^{-\left(\frac{t-t_b}{\tau_{\text{relax}}}\right)}\right].\end{aligned} \tag{10}$$

3. Escape from the surface

An additional energy loss occurs as the released photoelectron leaves the nanoparticle due to the increase of potential energy at the particle's surface. For the spherical square-well potential in our model, energy conservation requests the radial and tangential velocity components of the electron just before reaching the surface at $r = a$ ($v_{sr}^{(-)}$ and $v_{st}^{(-)}$, respectively) and just outside the surface ($v_{sr}^{(+)}$ and $v_{st}^{(+)}$, respectively) to be related according to

$$\begin{aligned}v_{sr}^{(+)} &= \sqrt{m^* v_{sr}^{(-)2} - 2V_0},\\ v_{st}^{(+)} &= \sqrt{m^*}\, v_{st}^{(-)}.\end{aligned} \tag{11}$$

The radial velocity $v_{sr}^{(-)}$ determines whether the electron is energetically able to leave the target and is thus of particular importance in our calculation of photoelectron spectra. Taking into account that electrons are released with a nonuniform distribution of initial velocities $\vec{v}_0$, which follows an assumed dipole distribution around the polarization direction of the XUV pulse, explains that the radial velocity component $v_{sr}^{(-)}$ tends to decrease for initial positions near the surface with increasing degree of latitude θ_{r_0}. This favors electron emission at the poles ($\theta_{r_0} = 0^\circ$ or 180°) and suppresses emission at the equator ($\theta_{r_0} = 90^\circ$). This effect is illustrated by the blue velocity vectors that are labeled with "1" in Fig. 4 and is referred to as "surface effect." The surface effect is thus expected to strongly suppress emission near the equator.

Emission from the equator is also subdued due to electron-transport effects as illustrated by the brown velocity vectors labeled "2" in Fig. 4. Moving the release point $\vec{r}_0$ on the surface from the pole to the equator, the propensity for long path lengths inside the particle increases, reducing the probability for electron emission and propagation toward the detector.

In addition to surface effects, transport effects noticeably influence photoelectron spectra. This is confirmed by our numerical applications and further discussed in Sec. III below.

4. Propagation to the detector

Assuming complete screening at the surface of the metallic nanosphere, escaping photoelectrons are subjected to (i) the incident IR and induced plasmonic electric field upon reaching the surface and (ii) a reduction of their mass from the effective value m^* to the free-electron mass $m = 1$. We calculate the final photoelectron velocity $\vec{v}_f^{\,\mathrm{det}}(\vec{r}_0,\vec{v}_0,\tau)$ by numerically solving the classical equation of motion

$$\frac{d}{dt}\vec{v}(\vec{r},t) = -\vec{E}_{\mathrm{inc}}(\vec{r},t) - \vec{E}_{\mathrm{pl}}(\vec{r},t), \quad r > a, \tag{12}$$

using a fourth-order Runge-Kutta method for a given time delay τ, initial position $\vec{r}_0$, and initial momentum $\vec{v}_0$. Not all emitted electrons reach the detector. In the numerical examples discussed below we count photoelectrons as detected if their final velocity direction lies within a cone about the positive z axis with an opening angle of $\theta_{\mathrm{acc}} = 45^\circ$.

C. Sampling trajectories

We include a large number of photoelectron trajectories by Monte Carlo sampling [38] over their initial phase-space points $(\vec{r}_0,\vec{v}_0)$. This sampling is carried out based on the probability density function (PDF) $\rho(\vec{r}_0,\vec{v}_0)$ that lends relative weights to the trajectories. Having described our calculation of individual trajectories in the previous section, we now detail our modeling of the PDF under the assumption that the initial photoelectron position $\vec{r}_0$ and velocity $\vec{v}_0$ are independent, allowing the separation

$$\rho(\vec{r}_0,\vec{v}_0) = \rho_{\mathrm{pos}}(\vec{r}_0)\rho_{\mathrm{vel}}(\vec{v}_0). \tag{13}$$

1. Initial positions

For the purpose of modeling $\rho_{\mathrm{pos}}(\vec{r}_0)$, we assume a constant electron density inside the nanosphere. Even though the charge redistribution on the nanoparticle surface by the streaking IR pulse creates a large plasmonic field, the number of electrons displaced by the action of the incident IR electromagnetic wave is negligible in comparison to the total number of free electrons in the conduction band. We can therefore safely suppose that the electron density remains uniformly distributed inside the nanosphere.

Consistent with our assumption made for the calculation of individual trajectories of the nanoparticle being transparent to the XUV pulse, we further assume that the XUV-photoemission rate is uniform inside the nanoparticle. This amounts to neglecting the macroscopic effect of the attenuation of the XUV pulse while (strictly speaking inconsistently) still allowing for XUV-triggered single-photon photoemission. Under these presuppositions, the PDF for initial positions is

$$\rho_{\mathrm{pos}}(\vec{r}_0) = \frac{1}{V}\begin{cases}1, & r_0 \leqslant a\\ 0, & r_0 > a.\end{cases} \tag{14}$$

2. Initial velocities

The velocity distribution resulting from the excitation of conduction electrons in the linearly polarized electric field of the XUV pulse is cylindrically symmetrical about the XUV polarization direction (z axis). Therefore, representing $\vec{v}_0$ in spherical coordinates, the PDF $\rho_{\mathrm{vel}}(\vec{v}_0) = \rho_{\mathrm{vel}}(v_0,\theta_{v_0})$ is independent of the azimuthal angle ϕ_{v_0}. Assuming that for the narrow range of photoelectron kinetic energies of relevance in our numerical applications below the initial photoelectron angular distribution does not depend on the electron speed v_0, we can separate v_0- and θ_{v_0}-dependent contributions to the velocity PDF, such that

$$\rho_{\mathrm{vel}}(\vec{v}_0) = \frac{1}{2\pi v_0^2 \sin(\theta_{v_0})}\rho_v(v_0)\rho_\theta(\theta_{v_0}). \tag{15}$$

The angle-dependent factor $\rho_\theta(\theta_{v_0})$ reflects the angular distribution of photoelectrons due to single-photon emission. For the assumed dipolar distribution the normalized PDF in θ_{v_0} is

$$\rho_\theta(\theta_{v_0}) = \frac{4}{\pi}\cos^2(\theta_{v_0}), \tag{16}$$

which immediately follows by applying Fermi's golden rule to single-photon electron emission from initial zero-angular-momentum atomic states [26]. We note that, since the detector is placed along the positive z axis, photoelectrons with final velocities along the negative z axis are not detected. Disregarding the very small chance of large-angle deflections of released photoelectrons inside the nanoparticle and in the external IR electromagnetic field, we restrict θ_{v_0} to the interval $[0,\pi/2]$ and normalize $\rho_\theta(\theta_{v_0})$ over this interval.

We determine $\rho_v(v_0)$ within the free-electron-gas model for conduction-band (CB) electrons [39], based on the electronic density of states

$$\rho_{\mathrm{CB}}(\varepsilon_{\mathrm{CB}}) = f_{\mathrm{FD}}(\varepsilon_{\mathrm{CB}})\tfrac{3}{2}\varepsilon_F^{-\frac{3}{2}}\sqrt{\varepsilon_{\mathrm{CB}}} \tag{17}$$

with the Fermi-Dirac (FD) distribution function

$$f_{\mathrm{FD}}(\varepsilon_{\mathrm{CB}}) = \frac{1}{\exp[(\varepsilon_{\mathrm{CB}} - \mu)/k_B T] + 1} \tag{18}$$

and conduction-electron energy $\varepsilon_{\mathrm{CB}}$. Neglecting the small change of the overall electron-kinetic-energy distribution at room temperature relative to $T = 0$ K, we assume $T = 0$ K, i.e.,

$$\rho_{\mathrm{CB}}(\varepsilon_{\mathrm{CB}}) = \begin{cases}\frac{3}{2}\varepsilon_F^{-\frac{3}{2}}\sqrt{\varepsilon_{\mathrm{CB}}}, & 0 \leqslant \varepsilon_{\mathrm{CB}} \leqslant \varepsilon_F\\ 0, & \text{otherwise.}\end{cases} \tag{19}$$

The squared Fourier transformation of Eq. (1) results in the spectral profile of the XUV pulse, which, upon normalization over all XUV photon energies $\varepsilon_{\mathrm{xuv}} > 0$, turns into the PDF

$$\rho_{\mathrm{xuv}}(\varepsilon_{\mathrm{xuv}}) = \left(\frac{2}{\pi\sigma_{\mathrm{xuv}}^2}\right)^{\frac{1}{2}}\exp\left(-\frac{\left(\varepsilon_{\mathrm{xuv}} - \varepsilon_{\mathrm{xuv}}^{\mathrm{ctr}}\right)^2}{2\sigma_{\mathrm{xuv}}^2}\right), \tag{20}$$

with the standard deviation $\sigma_{\mathrm{xuv}} = 1/\Delta t_{\mathrm{xuv}} = 2.7$ eV corresponding to the XUV spectral width (FWHIM) of 6.35 eV.

Since $\rho_{\mathrm{CB}}(\varepsilon_{\mathrm{CB}})$ and $\rho_{\mathrm{xuv}}(\varepsilon_{\mathrm{xuv}})$ are independent distributions, their convolution results in the PDF for XUV-excited

photoelectrons

$$\rho_{\mathrm{CB,xuv}}(\varepsilon^*_{\mathrm{CB}}) = \int_0^\infty d\varepsilon_{\mathrm{CB}} \rho_{\mathrm{CB}}(\varepsilon_{\mathrm{CB}}) \rho_{\mathrm{xuv}}(\varepsilon^*_{\mathrm{CB}} - \varepsilon_{\mathrm{CB}}), \quad (21)$$

where the energy of the excited CB photoelectron is given by $\varepsilon^*_{\mathrm{CB}} = \varepsilon_{\mathrm{CB}} + \varepsilon_{\mathrm{xuv}}$ (Fig. 2). The dispersion relation $v_0 = (2\varepsilon^*_{\mathrm{CB}}/m^*)^{1/2}$ for excited CB electrons inside the nanoparticle now leads to the PDF for the magnitude of the photoelectron velocity immediately after XUV excitation,

$$\begin{aligned}\rho_v(v_0) &= \int d\varepsilon^*_{\mathrm{CB}} \rho_{\mathrm{CB,xuv}}(\varepsilon^*_{\mathrm{CB}}) \delta(v_0 - \sqrt{2\varepsilon^*_{\mathrm{CB}}/m^*}) \\ &= m^* v_0 \rho_{\mathrm{CB,xuv}}\left(\tfrac{1}{2} m^* v_0^2\right). \end{aligned} \quad (22)$$

3. Monte Carlo sampling

In Sec. II B 2 we included transport effects in the calculation of individual photoelectron trajectories in terms of the IMFP λ_i. This results in the deceleration of the released electron inside the nanoparticle [cf. Eq. (10)]. Since the deceleration and change of propagation direction inside the nanoparticle affects the electron-detection probability, the PDF needs to take into account the effective loss of photoelectrons due to collisions. We incorporate the effects of the change in propagation direction and energy loss in terms of the relative probability of escape

$$\rho_l(l) = \frac{\exp[-l(\vec{r}_0,\vec{v}_0)/\lambda_i]}{\lambda_i\left[1 - \exp\left(-\frac{2a}{\lambda_i}\right)\right]} \quad (23)$$

that depends on the distance $l(\vec{r}_0,\vec{v}_0)$ the photoelectron covers inside the nanoparticle before reaching its surface and on λ_i. We thus count excited electrons that change their direction of propagation due to collisions as lost, i.e, as either being able to escape from the nanoparticle without reaching the detector or as not being able to escape. This implies that photoelectrons which are released farther away from the surface tend to have a lower probability to be emitted from the nanosphere.

Combing the transport effects as described in Eq. (22) with Eqs. (13) and (14) leads to the effective phase-space PDF

$$\rho_{\mathrm{tot}}(\vec{r}_0,\vec{v}_0) = \rho(\vec{r}_0,\vec{v}_0)\rho_l(l). \quad (24)$$

The distribution of observable final photoelectron velocities $\vec{v}_f = (v_f,\theta_{v_f},\phi_{v_f})$ is obtained from ρ_{tot} and the final asymptotic electron velocities $\vec{v}_f^{\,\mathrm{det}}(\vec{r}_0,\vec{v}_0,\tau)$ as

$$\rho_f(\vec{v}_f,\tau) = \iint d\vec{r}_0 d\vec{v}_0 \rho_{\mathrm{tot}}(\vec{r}_0,\vec{v}_0)\delta\left[\vec{v}_f - \vec{v}_f^{\,\mathrm{det}}(\vec{r}_0,\vec{v}_0,\tau)\right]. \quad (25)$$

From this expression we obtain the streaked photoemission spectra, i.e., the photoelectron yield

$$Y(K_f,\tau) = N v_f \int_{-\theta_{\mathrm{acc}}/2}^{\theta_{\mathrm{acc}}/2} \sin\theta_{v_f} d\theta_{v_f} \int_0^{2\pi} d\phi_{v_f} \rho_f(\vec{v}_f,\tau) \quad (26)$$

as a function of the final photoelectron kinetic energy $K_f = \frac{1}{2}v_f^2$ and the delay τ. With the factor

$$N = \left[\max_{K_f,\tau} Y(K_f,\tau)\right]^{-1} \quad (27)$$

we normalize the streaked photoelectron spectrum to its maximal yield.

III. NUMERICAL RESULTS AND DISCUSSION

In this section we are going to characterize the plasmonic field near the surface of the nanosphere by examining streaked photoelectron *spectra* and streaking *curves*. We represent streaked spectra as color-coded graphs of the normalized photoelectron yield $Y(K_f,\tau)$ [Eq. (26)]. We numerically evaluate Eq. (26) for fixed delays by binning final photoelectron kinetic energies resulting from trajectory calculations, $K_f^{\mathrm{det}} = \frac{1}{2}\vec{v}_f^{\,\mathrm{det}}(\vec{r}_0,\vec{v}_0,\tau)^2$, in small equidistant kinetic energy intervals of width $\Delta K_f = 0.6$ eV. For every spectrum we sample over 6 633 000 trajectories and compose the photoelectron yield as a histogram based on the kinetic energy bins. All spectra are calculated for a detector acceptance angle of $\theta_{\mathrm{acc}} = 45^\circ$. In our numerical studies we found that typically about 50% of the included trajectories contribute to the detected electron yield. The large number of not-"detected" trajectories is due to photoelectrons failing to reach the acceptance cone of the detector.

We refer to streaking *curves* as graphs of the photoelectron kinetic energy $K_f^{\mathrm{det}}(\vec{r}_0,\vec{v}_0,\tau) = \frac{1}{2}\vec{v}_f^{\,\mathrm{det}}(\vec{r}_0,\vec{v}_0,\tau)^2$ resulting from a single initial point inside the nanoparticle $\vec{r}_0$ and from a given initial velocity $\vec{v}_0$ as a function of τ. Since streaked spectra can be understood as the superposition of streaking curves, we discuss streaking curves with emphasis on the degree of spatial resolution at which streaking spectroscopy allows the imaging of plasmonic fields.

A. Emission-position dependence

1. Emission-depth dependence

Figure 5(a) shows streaking curves $K_f^{\mathrm{det}}(\vec{r}_0,\vec{v}_0,\tau)$ for $a =$ 50 nm gold nanospheres obtained from electron trajectories that start at the detector-facing pole $\vec{r}_p(0,0,a)$ for five different radial distances r_0 between 45 and 50 nm. The electrons are assumed to be emitted from the Fermi level with emission direction $\theta_{v_0} = 0^\circ$. The diagonal shift of the curves suggests that photoelectrons reach the detector with an increasing energy loss and time delay when r_0 moves from the surface towards the center of the nanosphere. These are expected manifestations of the transport effect discussed in Sec. II B 2: Photoelectrons which are excited deeper inside the nanoparticle require more time to reach the surface, causing an increasing time delay in the streaking curves. The delay difference amounts to 0.85 fs between electrons that start at $r_0 = 50$ and 45 nm. In addition, the increasing path length inside the nanosphere increases the chance for photoelectrons experiencing collisions during their transport to the surface, causing the likewise increasing kinetic energy loss. Relative to trajectories that start at the surface ($r_0 = 50$ nm), the energy loss depicted in the streaking curve amounts to 6 eV if the release point is shifted to $r_0 = 45$ nm.

The streaking curves in Fig. 5(b) are calculated for the same five release points and emission from the Fermi level only as in Fig. 5(a). However, the initial photoelectron velocity directions are selected randomly for each delay τ and weighted with the dipole distribution (16). By randomizing the velocity directions, photoelectrons acquire different path lengths inside the nanoparticle, resulting in different escape probabilities and

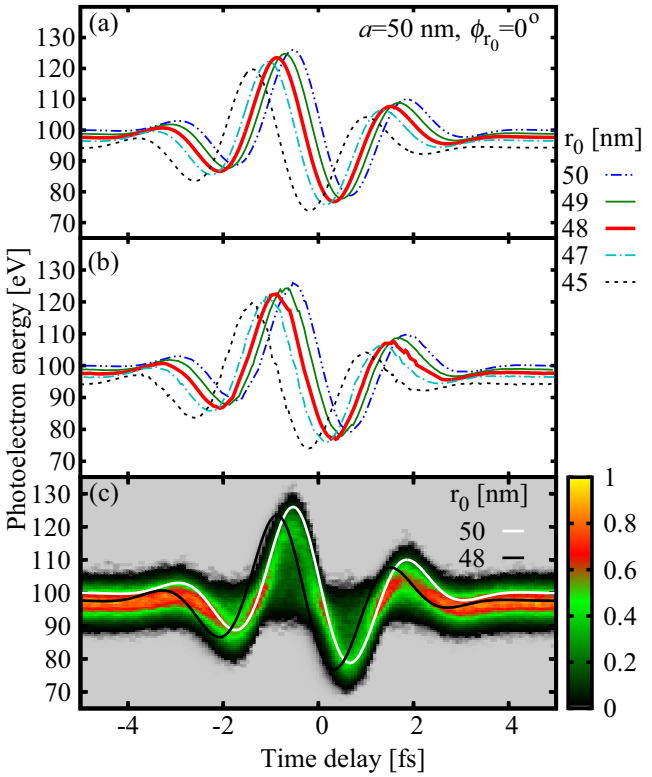

FIG. 5. Streaking curves and streaked spectrum from 50-nm Au nanospheres. (a) Streaking curves for photoelectrons emitted from the Fermi level with emission direction $\theta_{v_0} = 0^\circ$ from five release points $(r_0, \theta_{r_0} = 0^\circ)$ located on an axis joining the detector-facing pole and center of the nanosphere. (b) Streaking curves for the same five points and emission from the Fermi level for randomized velocity directions θ_{v_0}. (c) Simulated streaked spectrum and two streaking curves from release points $(r_0 = 50, \theta_{r_0} = 0^\circ)$ (white curve) and $(r_0 = 48, \theta_{r_0} = 0^\circ)$ (black curve). The spectrum is calculated for emission from the entire occupied conduction band, while the two streaking curves are calculated for emission from the Fermi level only. The spectrum is normalized to its maximal yield. The assumed emission direction for the two streaking curves is $\theta_{v_0} = 0^\circ$.

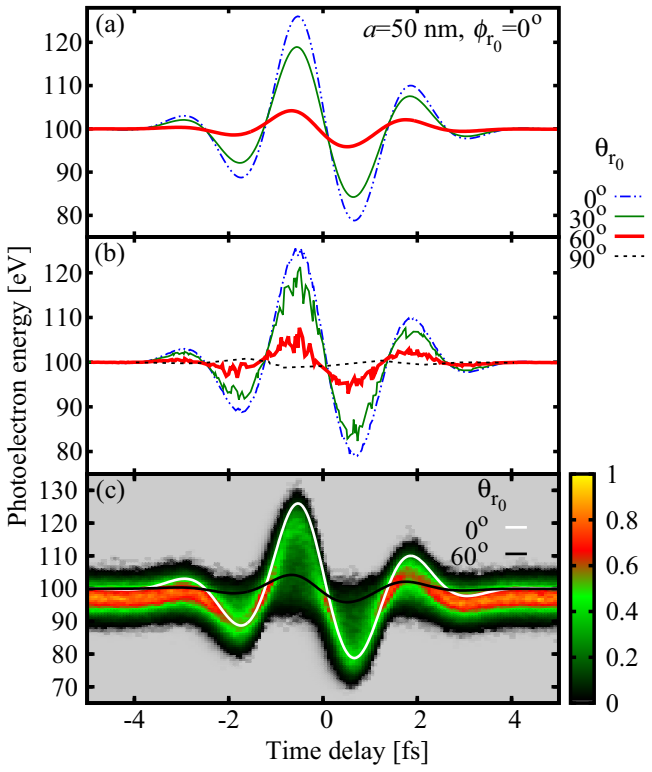

FIG. 6. Streaking curves and streaked spectra from 50-nm Au nanospheres. (a) Streaking curves for photoelectrons emitted from the Fermi level with emission direction $\theta_{v_0} = 0^\circ$ for four emission latitudes θ_{r_0} between the pole and equator on the nanosphere surface. (b) As (a) for randomized velocity directions θ_{v_0}. (c) Simulated streaked spectrum and two streaking curves from release points $(r_0 = a, \theta_{r_0} = 0^\circ)$ (white curve) and $(r_0 = a, \theta_{r_0} = 60^\circ)$ (black curve). The spectrum is calculated for emission from the entire occupied conduction band, while the two streaking curves are calculated for emission from the Fermi level only. The spectrum is normalized to its maximal yield. For the two streaking curves the assumed emission direction is $\theta_{v_0} = 0^\circ$.

energy losses that explain the appearance of small fluctuations in the streaking curves. As expected, these fluctuations become more pronounced as the release point is shifted towards the nanosphere center. The fact that even after velocity-direction randomization we basically get the same streaking curves for each initial position indicates that every radial emission point uniquely translates into a corresponding streaking curve.

Figure 5(c) shows how two individual streaking curves for emission from the Fermi level and surface of 50-nm-radius gold nanospheres with emission direction $\theta_{v_0} = 0^\circ$ from initial points $(r_0 = 50, \theta_{r_0} = 0^\circ)$ and $(r_0 = 48, \theta_{r_0} = 0^\circ)$ contribute to the streaked spectrum. This graph illustrates that streaked spectra contain (radial) spatial information in addition to temporal information.

2. *Emission-angle dependence*

Figures 6(a) and 7(a) show streaking curves for four release points on the nanosphere surface $(r_0 = a)$ at different latitudes θ_{r_0} between the detector-facing pole and equator of the sphere for emission from the Fermi level with emission direction $\theta_{v_0} = 0^\circ$. Figures 6 and 7 show results for radii of 50 and 5 nm, respectively. The striking decrease of the streaking oscillation amplitude for increasing θ_{r_0} is due to the inhomogeneous plasmonic field being the strongest at the pole and decreasing in strength towards the equator of the nanosphere. The absence of streaking curves for $\theta_{r_0} = 90^\circ$ in Figs. 6(a) and 7(a) is due to the released photoelectrons having insufficient kinetic energy to overcome the potential barrier at the nanosphere surface (surface effect) and transport effects.

The streaking curves in Figs. 6(b) and 7(b) are calculated for the same four points and for emission from the Fermi level as the curves in Figs. 6(a) and 7(a), respectively, but for randomized velocity directions. As in Fig. 5(b) above, the fluctuations in Figs. 6(b) and 7(b) are due to velocity randomization. As θ_{r_0} increases, moving from the pole towards the equator, the fluctuations increase due to the increasing transport path lengths $l(\vec{r}_0, \vec{v}_0)$ and energy loss that photoelectrons experience before reaching the surface. The fact that velocity randomization does not change the overall shape of the streaking curves indicates that, for emission from the surface,

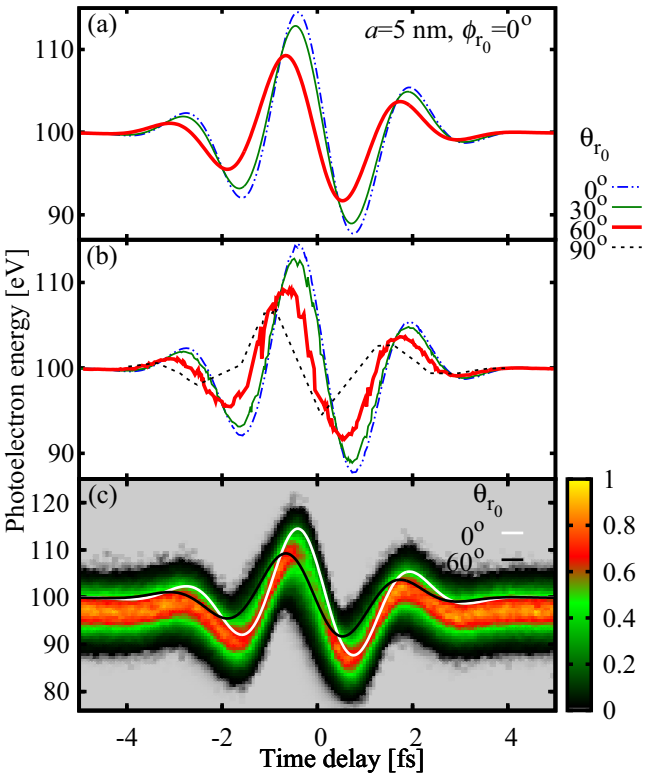

FIG. 7. As Fig. 6 for 5-nm Au nanospheres.

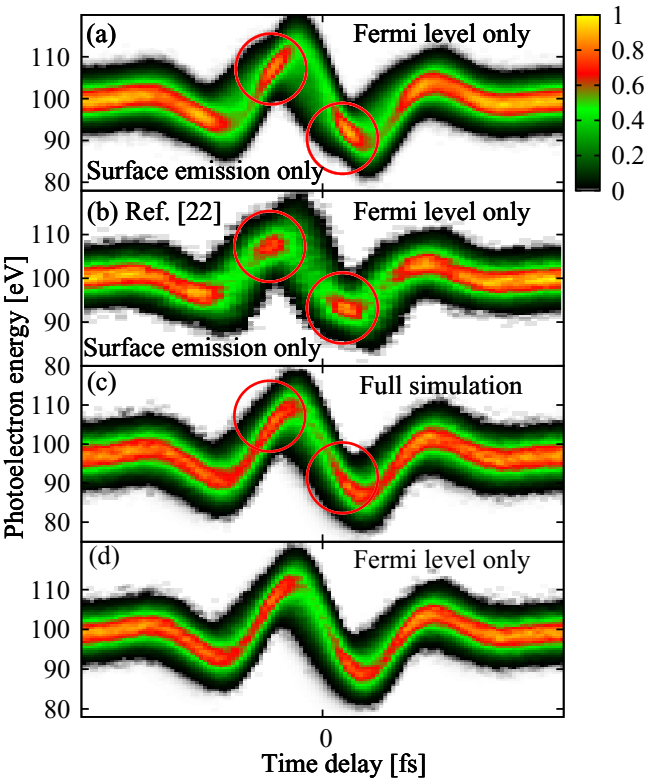

FIG. 8. Simulated streaked spectra for $a = 5$-nm-radius Au nanospheres normalized individually to their maximal yields. (a) Restricted sampling over particle surface and Fermi level only. (b) Adapted from Ref. [22]. (c) Full simulation, including sampling over the occupied conduction band, the XUV-pulse spectral profile, and the volume of the nanoparticle. (d) As (c) for emission from the Fermi level only (without sampling over the conduction band).

every emission latitude is associated with a streaking curve. Since larger nanospheres allow for longer propagation path lengths inside the particle, the fluctuations for 50-nm-radius spheres in Fig. 6(b) are more pronounced than for 5-nm-radius spheres in Fig. 7(b).

Figures 6(c) and 7(c) show the contribution of two individual streaking curves to the streaked spectrum for 50- and 5-nm radii, respectively. These streaking curves are calculated for electrons emitted from the Fermi level at release points ($r_0 = a, \phi_{r_0} = 0°, \theta_{r_0} = 0°$) and ($r_0 = a, \phi_{r_0} = 0°, \theta_{r_0} = 60°$). They show that streaked spectra contain angular spatial information in addition to radial spatial and temporal information.

Our study of the emission-depth and emission-angle dependence suggests that each emission point $\vec{r}_0$ is mapped on a corresponding streaking curve which contributes to the streaked spectrum. Therefore, in addition to temporal we expect streaked photoelectron spectra to allow the distinction of local emission characteristics and the plasmonic-field distribution near the nanosphere surface with some degree of spatial resolution. If we consider streaked spectra as the sum of all streaking curves with a weight function that depends on the path length $l(\vec{r}_0, \vec{v}_0)$, we can relate high electron yields to high densities of streaking curves. Delays at which streaking curves intersect thus tend to correspond to large photoelectron yields. This is confirmed by comparing the streaking curves in Figs. 5, 6, and 7 with the respective spectra in Figs. 5(c), 6(c), and 7(c).

B. Conduction-band, surface, and transport effects

The spectra shown in Figs. 6(c) and 7(c) are obtained for "full" simulations, including electron emission from the entire occupied part of the conduction band, and after sampling over release points $(\vec{r}_0, \vec{v}_0)$ in the nanosphere ($r_0 \leqslant a$). In this section, we investigate the effects of restricting the release locations and initial energy of the photoelectrons. Figure 8(a) is generated by sampling over the XUV spectral energy profile, assuming that all photoelectrons are emitted from the Fermi level only and released from the surface ($r_0 = a$) by the XUV pulse. Classical simulations with the same restrictions on the initial energy and release location of the active electron were performed earlier in Ref. [22] and are shown in Fig. 8(b) to be in good overall agreement with our result.

We extended the model suggested in Ref. [22] by (i) representing the conduction band as a spherical square-well potential, thereby including the surface effect, (ii) sampling over the entire conduction bandwidth, and (iii) sampling not only over electron trajectories that initiate at the surface, by adding photoelectrons released inside the nanoparticle, thus including transport effects. Each of these extensions has a noticeable impact on streaked spectra. The spectrum in Fig. 8(c) shows results of our full simulation, including all of the above extensions. We generated Fig. 8(d) under the same assumptions as Fig. 8(c), but without sampling over the conduction bandwidth, assuming emission from the Fermi level only.

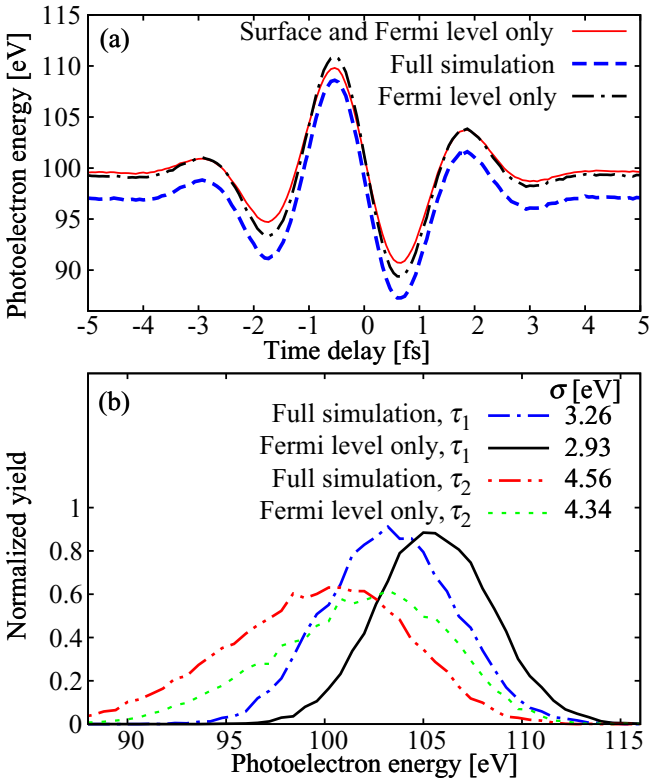

FIG. 9. (a) Centers of energy for the spectra in Figs. 8(a), 8(c), and 8(d). (b) Energy profiles of the spectra in Figs. 8(c) and 8(d) for time delays $\tau_1 = -933$ as and $\tau_2 = 0$ as and corresponding spectral widths (standard deviations) σ.

The comparison of Figs. 8(c) and 8(d) reveals that the inclusion of initial states from the entire occupied conduction band shifts the center of energy (COE) of the streaking trace to lower energies, as expected with regard to energy conservation. This downward energy shift amounts to $\Delta_{\mathrm{COE}} = 2.22$ eV. Within the free-electron-gas model [Eq. (19)] for the gold conduction band, Δ_{COE} is related to the average conduction-band energy $\langle \varepsilon_{\mathrm{CB}} \rangle$ according to

$$\Delta_{\mathrm{COE}} = \varepsilon_F - \langle \varepsilon_{\mathrm{CB}} \rangle = \tfrac{2}{5}\varepsilon_F. \tag{28}$$

This allows the retrieval of the Fermi energy from our simulated streaked spectra as $\varepsilon_F = \frac{5}{2}\Delta_{\mathrm{COE}} = 5.50$ eV, in good agreement with the theoretical value, $\varepsilon_F = 5.53$ eV, of Ref. [27].

The superimposed circles in Figs. 8(a), 8(b), and 8(c) highlight two delay ranges with high detected photoelectron yields. These intervals coincide with particularly high densities and intersections of streaking curves in Figs. 7(a) and 7(b). The large contrast in electron yield seen in Figs. 8(a) and 8(b) is reduced in Figs. 8(c) and 8(d). This is due to the reduction of the detectable electron yield as a result of the surface and transport effects we discussed earlier.

Figure 9(a) shows COEs for emission from the surface and Fermi level only, for our full simulation and for emission from the Fermi level only. These COE curves correspond to the spectra in Figs. 8(a), 8(c), and 8(d), respectively. The COE for emission from the Fermi level only has a larger oscillation amplitude than the COE for emission from the surface and Fermi level only. This is a result of the smaller yield of photoelectrons that are released close to the equator and a consequence of the surface and transport effects.

Since both photoelectron current and induced plasmonic field are the strongest at the pole and decrease towards the equator, photoelectrons, on average, acquire larger streaking energy shifts if more electrons are emitted near the pole than near the equator. This is the case when the restriction for emission from the surface only is lifted and emission from the volume is included. The streaking amplitude for emission from the Fermi level only is therefore larger than for emission from the surface only and Fermi level only, as the comparison of the black dash-dotted and solid red COE curves in Fig. 9(a) demonstrates. Going from surface to volume emission also induces a small shift of the COE towards lower energies, due to energy loss during electron transport to the surface. For emission from the Fermi level only, this COE shift amounts to 0.3 eV. One might, in addition, expect a phase shift to be associated with the addition of volume emission. However, we do not observe a noticeable phase shift for the numerical examples discussed in this work. Larger phase shifts might occur in poor conductors with smaller relaxation times τ_{relax}.

In Fig. 9(b) we compare the spectral profiles of spectra for two different time delays. As indicated by the superimposed circles in Fig. 8 delays $\tau_1 = -933.3$ as and $\tau_2 = 0$ correspond to high and low photoemission yields, respectively. These profiles, and thus the corresponding temporal profiles of the photoelectron wave packet, are different. Allowing for emission from the entire occupied conduction band (full simulation) leads to a slightly larger energetic width of the spectra. This is quantified in terms of their standard deviations σ in the legend of Fig. 9(b).

C. Plasmonic effects

The effects of the induced plasmonic fields on streaked electron emission are addressed in Fig. 10 for nanospheres with radii of 50 nm (left column) and 5 nm (right column) and for streaking-pulse wavelengths of 720 nm [Figs. 10(a)–10(d)] and 530 nm [Figs. 10(e)–10(h)]. Figures 10(c), 10(d), 10(g), and 10(h) show spectra that are calculated without including the plasmonic field $\vec{E}_{\mathrm{pl}}$ given by Eq. (4). The comparison of streaked spectra from full simulations, including the plasmonic field in Figs. 10(a), 10(b), 10(e), and 10(f), with those that do not include $\vec{E}_{\mathrm{pl}}$ for a given nanosphere radius and streaking wavelength reveals a significant increase of the streaking amplitudes due to the plasmonic-field enhancement of the streaking electric field. For both wavelengths the increase in streaking amplitude is larger for 50-nm-radius spheres than for 5-nm-radius spheres, as expected, since the plasmonic-field enhancement for 50-nm spheres is larger (cf. Fig. 3).

For gaseous atomic targets and for laser- and XUV-pulse parameters realized in typical streaking experiments, it is well known that the streaking amplitude is proportional to the wavelength and amplitude of the incident IR field [18]. However, this proportionality does not necessarily apply to nanospheres, as the comparison of Figs. 10(a) and 10(b) with Figs. 10(e) and 10(f), respectively, demonstrates. Instead, for both 50- and 5-nm-radius nanospheres, the streaking

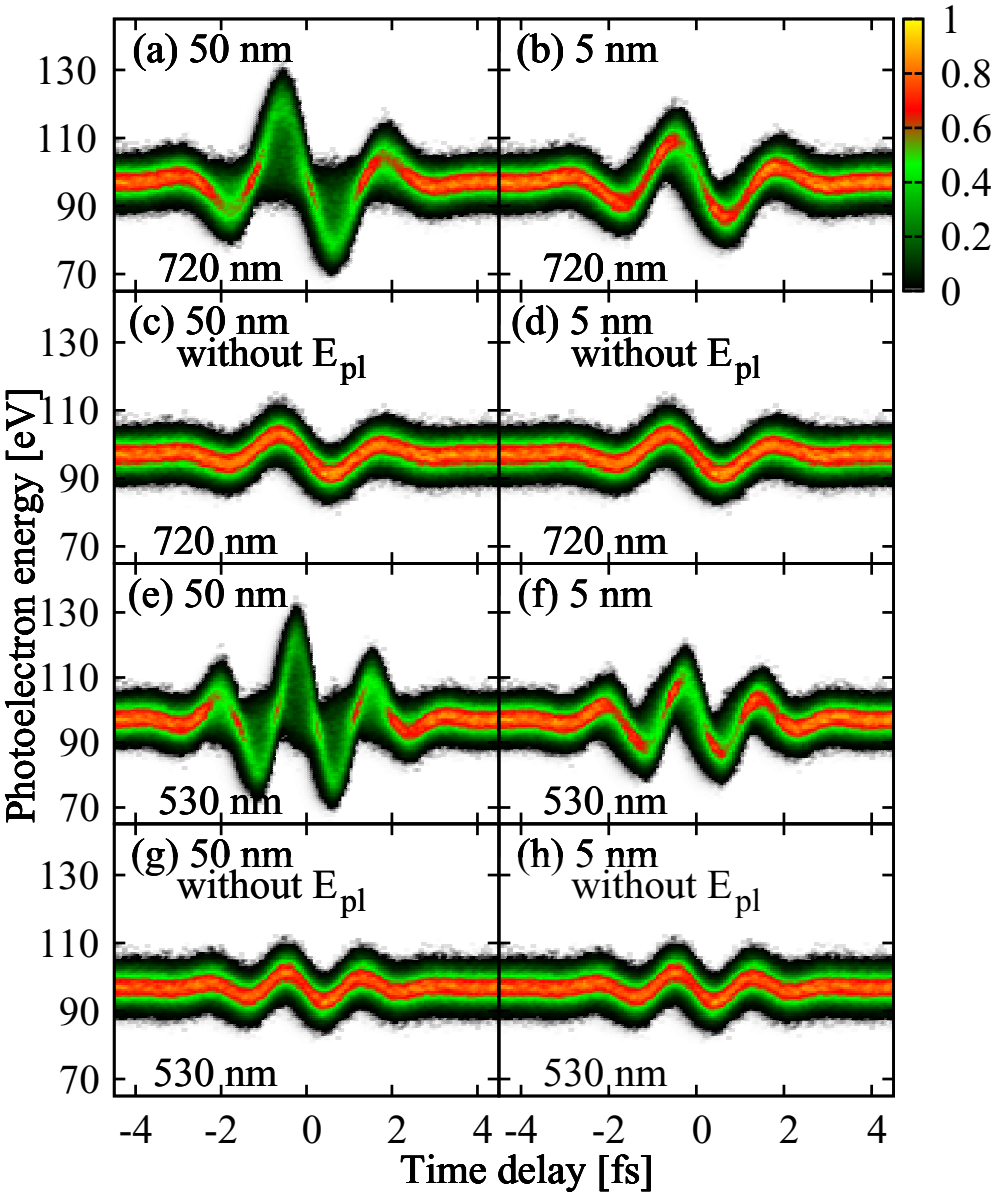

FIG. 10. Streaked spectra from Au nanospheres for streaking-pulse wavelengths of (a)–(d) 720 nm and (e)–(h) 530 nm, with radii of [(a), (c), (e), and (g)] 50 nm and [(b), (d), (f), and (h)] 5 nm. The spectra are normalized individually to their maximal yields. Results from full simulations that [(a), (b), (e), and (f)] include and [(c), (d), (g), and (h)] do not take into account the plasmonic field $\vec{E}_{\rm pl}$ [Eq. (4)].

amplitudes for 530- and 720-nm streaking pulses are approximately equal. The deviation from the expected proportionality observed for gaseous atomic targets is another manifestation of plasmonic-field enhancement and due to the streaking-wavelength dependence of the plasmonic-field amplitude near the nanosphere surface. Maximal field enhancement occurs near the surface-plasmon-resonance wavelengths which are 541 and 530 nm for 50- and 5-nm Au nanospheres, respectively (Fig. 3). Therefore, the lack of a reduced streaking amplitude at 530-nm streaking wavelength is due to the increased plasmonic-field enhancement at 530 nm. While the approximate cancellation of the expected wavelength dependence by the wavelength-dependent plasmonic-field enhancement is coincidental for the two streaking wavelengths we compared in Fig. 10, this comparison shows that, in general, the amplitude of streaked spectra from metallic nanoparticles sensitively depends on their wavelength-dependent dielectric response.

Figure 11 shows the COEs corresponding to the spectra in Fig. 10. COEs including plasmonic-field enhancement are represented by solid black curves and the ones excluding field enhancement by dash-dotted red curves. In addition to the wavelength- and size-dependent streaking amplitudes, the COEs reveal wavelength- and size-dependent phase shifts that are induced by the plasmonic field. As shown in a previous quantum-mechanical calculation [12], the scrutiny of COE amplitudes and phase shifts allows the quantitative retrieval of the plasmonic-field enhancement with high accuracy. For a given wavelength, the spectra from the larger nanosphere have larger COE amplitudes. For a given radius, the COE

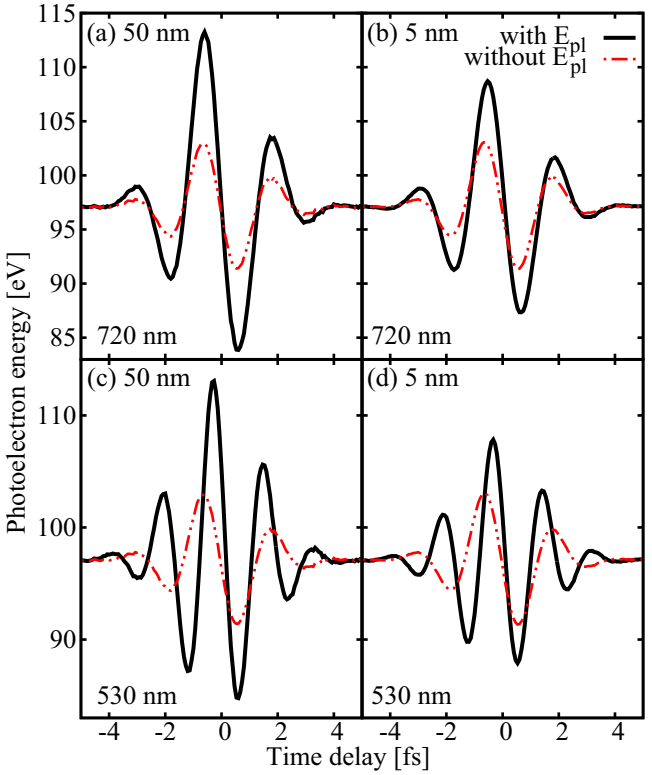

FIG. 11. Center-of-energy curves for streaking wavelengths of 720 and 530 nm and nanosphere radii of 50 and 5 nm for the streaked spectra in Fig. 10. Results including and excluding nanoplasmonic-field enhancement are shown as solid black and dash-dotted red curves, respectively.

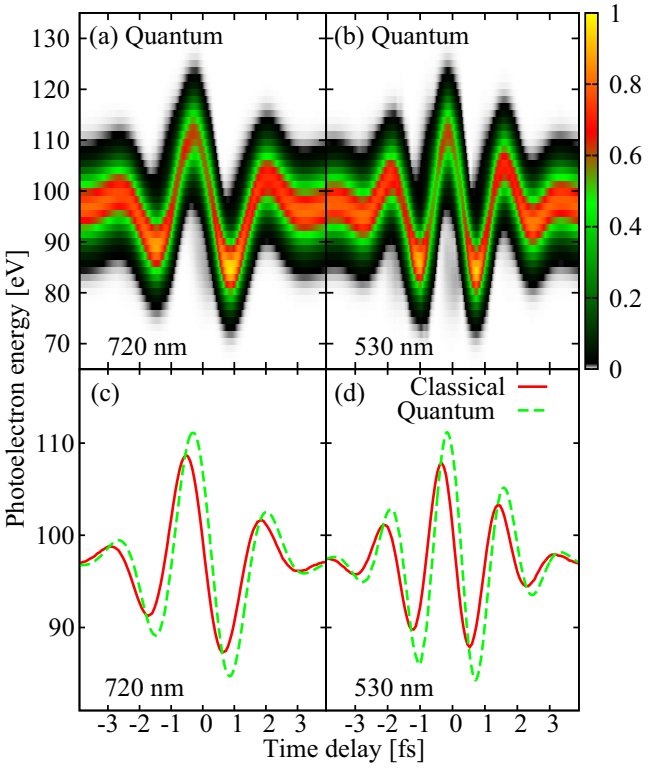

FIG. 12. Simulated streaked spectra from 5-nm Au nanospheres individually normalized to their maximal yields for streaking-pulse wavelengths of (a) 720 nm and (b) 530 nm according to the quantum-mechanical model of Ref. [12]. [(c) and (d)] Corresponding centers of energy for the classically simulated spectra in Figs. 10(b) and 10(f) (solid red line) and the spectra in (a) and (b) (green dashed line).

amplitudes for 720- and 530-nm streaking wavelength are almost equal, consistent with the discussion of Fig. 10 above.

D. Comparison with quantum-mechanical simulations

Figures 12(a) and 12(b) show quantum-mechanically calculated streaked photoemission spectra for 5-nm-radius gold nanospheres and two streaking wavelengths of Ref. [12]. These two graphs are generated for the same streaking-field and XUV-pulse parameters as our corresponding classically calculated spectra in Figs. 10(b) and 10(f). The quantum-mechanical and classical spectra are in reasonable overall agreement, but differ with regard to the spectral distributions along the streaking traces. The quantum-mechanical results show slightly larger variations in the spectrally resolved electron yield as a function of the time delay. The smaller delay-dependent variance in electron yield (streaking amplitude) predicted in our classical simulation is consistent with our XUV-photon-energy-independent modeling of the photoelectron release process, while the quantum-mechanical calculation in Ref. [12] is based on XUV-photon-energy-dependent photoemission amplitudes.

In order to allow for a quantitative comparison, we show in Figs. 12(c) and 12(d) the COEs for the spectra in Figs. 10(b), 10(f), 12(a), and 12(b). Their comparison reveals slightly larger streaking amplitudes for the quantum-mechanical calculation and a phase shift between the classically and quantum-mechanically computed streaking traces.

IV. CONCLUSION

We developed a classical model to study attosecond streaking spectroscopy from metallic nanospheres, extending a previous classical model by sampling over the entire conduction band and including transport and surface effects. Our numerical results show that these extensions noticeably impact streaking spectra. By varying the radius of the nanosphere and the wavelength of the streaking pulse, and adding or relaxing restrictions to emission from the Fermi level only and from the surface of the nanoparticle only, we scrutinized streaked photoemission spectra. In particular, we addressed (i) the influence of the nanoparticle's dielectric response on streaked photoemission and (ii) the fidelity with which streaked spectra allow the imaging of the temporal and spatial distribution of the nanoparticle's induced plasmonic near field. The developed classical model is basic and versatile. It can be transferred to different geometries, such as surfaces [40,41], nanowires [42], nanotips [43], and metal and semiconductor nanostructures [11,44].

ACKNOWLEDGMENTS

This work was supported in part by the NSF Experimental Program to Stimulate Competitive Research (EPSCoR)

(including funds for investigating laser induced electric-field enhancement near nanostructures), NSF Grant No. PHY 1464417 (including theory development for photoemission from surfaces), and the Chemical Sciences, Geosciences, and Biosciences Division, Office of Basic Energy Sciences, Office of Science, U.S. DOE (including attosecond interferometry and photoemission from atoms in spatially varying external fields).

[1] S. R. Leone, C. W. McCurdy, J. Burgdörfer, L. S. Cederbaum, Z. Chang, N. Dudovich, J. Feist, C. H. Greene, M. Ivanov, R. Kienberger, U. Keller, M. F. Kling, Z.-H. Loh, T. Pfeifer, A. N. Pfeiffer, R. Santra, K. Schafer, A. Stolow, U. Thumm, and M. J. J. Vrakking, Nat. Photon. **8**, 162 (2014).
[2] F. Krausz and M. I. Stockman, Nat. Photon. **8**, 205 (2014).
[3] E. Hutter and J. H. Fendler, Adv. Mater. **16**, 1685 (2004).
[4] M. I. Stockman, M. F. Kling, U. Kleineberg, and F. Krausz, Nat. Photon. **1**, 539 (2007).
[5] A. Kinkhabwala, Z. Yu, S. Fan, Y. Avlasevich, K. Müllen, and W. Moerner, Nat. Photon. **3**, 654 (2009).
[6] S. L. Stebbings, F. Süßmann, Y. Y. Yang, A. Scrinzi, M. Durach, A. Rusina, M. I. Stockman, and M. F. Kling, New J. Phys. **13**, 073010 (2011).
[7] E. Skopalová, D. Lei, T. Witting, C. Arrell, F. Frank, Y. Sonnefraud, S. Maier, J. Tisch, and J. Marangos, New J. Phys. **13**, 083003 (2011).
[8] M. Becker, W. C.-W. Huang, H. Batelaan, E. J. Smythe, and F. Capasso, Ann. Phys. (Berlin) **525**, L6 (2013).
[9] S. Kim, J. Jin, Y.-J. Kim, I.-Y. Park, Y. Kim, and S.-W. Kim, Nature (London) **485**, E1 (2012).
[10] P. Dombi, A. Horl, P. Racz, I. Marton, A. Trugler, J. R. Krenn, and U. Hohenester, Nano Lett. **13**, 674 (2013).
[11] S. Zherebtsov, T. Fennel, J. Plenge, E. Antonsson, I. Znakovskaya, A. Wirth, O. Herrwerth, F. Süßmann, C. Peltz, I. Ahmad, S. A. Trushin, V. Pervak, S. Karsch, M. J. J. Vrakking, B. Langer, C. Graf, M. I. Stockman, F. Krausz, E. Ruhl, and M. F. Kling, Nat. Phys. **7**, 656 (2011).
[12] J. Li, E. Saydanzad, and U. Thumm, Phys. Rev. A **94**, 051401 (2016); **95**, 043423 (2017).
[13] M. I. Stockman, Phys. Today **64**(2), 39 (2011).
[14] S. I. Bozhevolnyi, J. Beermann, and V. Coello, Phys. Rev. Lett. **90**, 197403 (2003).
[15] E. Le Ru and P. Etchegoin, *Principles of Surface-Enhanced Raman Spectroscopy: And Related Plasmonic Effects* (Elsevier, Oxford, 2008).
[16] X. Zhang, Y. L. Chen, R.-S. Liu, and D. P. Tsai, Rep. Prog. Phys. **76**, 046401 (2013).
[17] M. T. Sheldon, J. Van de Groep, A. M. Brown, A. Polman, and H. A. Atwater, Science **346**, 828 (2014).
[18] U. Thumm, Q. Liao, E. M. Bothschafter, F. Süßmann, M. F. Kling, and R. Kienberger, *Fundamentals of Photonics and Physics* (Wiley, New York, 2015), Vol. 1, Chap. 13.
[19] C. Lemell, B. Solleder, K. Tőkési, and J. Burgdörfer, Phys. Rev. A **79**, 062901 (2009).
[20] Q. Liao and U. Thumm, Phys. Rev. Lett. **112**, 023602 (2014).
[21] C.-H. Zhang and U. Thumm, Phys. Rev. A **84**, 065403 (2011).
[22] F. Süßmann and M. F. Kling, Phys. Rev. B **84**, 121406 (2011).
[23] F. Kelkensberg, A. Koenderink, and M. Vrakking, New J. Phys. **14**, 093034 (2012).
[24] A. G. Borisov, P. M. Echenique, and A. Kazansky, New J. Phys. **14**, 023036 (2012).
[25] J. S. Prell, L. J. Borja, D. M. Neumark, and S. R. Leone, Ann. Phys. (Berlin) **525**, 151 (2013).
[26] E. Merzbacher, in *Quantum Mechanics* (Wiley, New York, 1998), p. 501.
[27] N. Ashcroft and N. Mermin, *Solid State Physics* (Saunders College, Philadelphia, 1976).
[28] W. M. Haynes, *CRC Handbook of Chemistry and Physics* (CRC Press, Boca Raton, FL, 2014).
[29] J. D. Jackson, *Classical Electrodynamics*, 3rd ed. (Wiley, New York, 1999).
[30] S. W. Verbruggen, M. Keulemans, J. A. Martens, and S. Lenaerts, J. Phys. Chem. C **117**, 19142 (2013).
[31] G. Mie, Ann. Phys. (Berlin) **330**, 377 (1908).
[32] H. Kuwata, H. Tamaru, K. Esumi, and K. Miyano, Appl. Phys. Lett. **83**, 4625 (2003).
[33] P. G. Etchegoin, E. Le Ru, and M. Meyer, J. Chem. Phys. **125**, 164705 (2006).
[34] A. Vial, T. Laroche, M. Dridi, and L. Le Cunff, Appl. Phys. A **103**, 849 (2011).
[35] S. A. Maier, *Plasmonics: Fundamentals and Applications* (Springer, New York, 2007).
[36] P. B. Johnson and R.-W. Christy, Phys. Rev. B **6**, 4370 (1972).
[37] S. Tanuma, C. Powell, and D. Penn, Surf. Interface Anal. **43**, 689 (2011).
[38] M. H. Kalos and P. A. Whitlock, *Monte Carlo Methods* (Wiley, Weinheim, 2008).
[39] C. Kittel, *Introduction to Solid State Physics* (Wiley, Hoboken, NJ, 2004).
[40] S. Neppl, R. Ernstorfer, A. Cavalieri, C. Lemell, G. Wachter, E. Magerl, E. Bothschafter, M. Jobst, M. Hofstetter, U. Kleineberg, J. V. Barth, D. Menzel, J. Burgdörfer, P. Feulner, F. Krausz, and R. Kienberger, Nature (London) **517**, 342 (2015).
[41] W. Okell, T. Witting, D. Fabris, C. Arrell, J. Hengster, S. Ibrahimkutty, A. Seiler, M. Barthelmess, S. Stankov, D. Lei, Y. Sonnefraud, M. Rahmani, T. Uphues, S. A. Maier, J. P. Marangos, and J. W. G. Tisch, Optica **2**, 383 (2015).
[42] C. Rewitz, T. Keitzl, P. Tuchscherer, J.-S. Huang, P. Geisler, G. Razinskas, B. Hecht, and T. Brixner, Nano Lett. **12**, 45 (2011).
[43] B. Förg, J. Schötz, F. Süßmann, M. Förster, M. Krüger, B. Ahn, W. Okell, K. Wintersperger, S. Zherebtsov, A. Guggenmos, V. Pervak, A. Kessel, S. A. Trushin, A. M. Azzeer, M. I. Stockman, D. Kim, F. Krausz, P. Hommelhoff, and M. F. Kling, Nat. Commun. **7**, 11717 (2016).
[44] M. Schultze, K. Ramasesha, C. Pemmaraju, S. Sato, D. Whitmore, A. Gandman, J. S. Prell, L. Borja, D. Prendergast, K. Yabana, D. M. Neumark, and S. R. Leone, Science **346**, 1348 (2014).